

Imaging and Analysis of Encapsulated Objects through Self-Assembled Electron and Optically Transparent Graphene Oxide Membranes

Alexander Yulaev^{1,2,3}, Alexey Lipatov⁴, Annie Xi Lu⁵, Alexander Sinitiski^{4,6}, Marina S. Leite^{2,7} and Andrei Kolmakov^{1}*

¹ Center for Nanoscale Science and Technology, NIST, 100 Bureau Drive, Gaithersburg, MD 20899-6204 USA

² Department of Materials Science and Engineering, University of Maryland, College Park, MD 20742 USA

³ Maryland NanoCenter, University of Maryland, College Park, MD 20742, USA

⁴ Department of Chemistry, University of Nebraska – Lincoln, Lincoln, NE 68588, USA

⁵ Department of Chemical & Biomolecular Engineering, University of Maryland, College Park, MD 20742-2111

⁶ Nebraska Center for Materials and Nanoscience, University of Nebraska – Lincoln, Lincoln, NE 68588, USA

⁷ Institute for Research in Electronics and Applied Physics, University of Maryland, College Park, MD 20742, USA

E-mail: andrei.kolmakov@nist.gov

Keywords: graphene oxide, encapsulation, scanning electron microscopy, histology, forensics

We demonstrate a technique for facile encapsulation and adhesion of micro- and nano objects on arbitrary substrates, stencils, and micro structured surfaces by ultrathin graphene oxide membranes via a simple drop casting of graphene oxide solution. A self-assembled encapsulating membrane forms during the drying process at the liquid-air and liquid-solid interfaces and consists of a water-permeable quasi-2D network of overlapping graphene oxide flakes. Upon drying and interlocking between the flakes, the encapsulating coating around the object becomes mechanically robust, chemically protective, and yet highly transparent to electrons and photons in a wide energy range, enabling microscopic and spectroscopic access to encapsulated objects. The characteristic encapsulation scenarios were demonstrated on a set of representative inorganic and organic micro and nano-objects and microstructured surfaces. Different coating regimes can be achieved by controlling the pH of the supporting solution, and the hydrophobicity and morphology of interfaces. Several specific phenomena such as compression of encased objects by contracting membranes as well as hierarchical encapsulations were observed. Finally, electron as well as optical microscopy and analysis of encapsulated objects along with the membrane effect on the image contrast formation, and signal attenuation are discussed

1. Introduction

The problems of object isolation from reactive environment and understanding the physics and chemistry of surface passivation are of great importance for a variety of applications such as microelectronics,^[1] drug delivery,^[2] forensics^[3], archeology/paleontology, and space research.^[4] In scientific practices, encapsulation of micro-objects in organic matrices is commonly used in histology.^[5] While, in general, encapsulation implies the protection of objects from undesirable effects of ambient conditions, the opposite is also true, and isolation can be important to protect the environment from hazardous effects of biologically or chemically reactive, toxic or radioactive nature of the encapsulated objects.^[6]

In addition to physicochemical protection of objects from the ambient, the ability to image and analyze the encapsulated matter spectroscopically is often a requirement. The latter becomes a challenge when the sampling area is reduced to meso- or nanoscale necessitating the application of electron, advanced optical or X-ray microscopies^[7]. In the light of the aforementioned requirements, nanometer-thin membranes and coatings made of low atomic number (*Z*) elements, such as graphene and graphene oxide (GO), were employed as electron

transparent windows for *in situ* ambient pressure electron microscopy^[8] and optical as well as X-ray spectroscopy due to their high transparency to both photons^[9] and electrons in a wide energy range^[10]. Graphene oxide colloids have a peculiar combination of properties and can serve a prospective material platform for high yield fabrication of encapsulating membranes^[11] with the following advantages: (i) amphiphilic nature of individual colloid particles^[11c], (ii) unimpeded water permeability of hydrated membranes^[12], and (iii) mechanical stiffness upon drying^[11b]. Indeed, during mechanical tests values of the tensile strength exceeding 30 GPa were reported for the dry membranes^[11b], implying that individual micro flakes are strongly interlocked inside the membrane. As it has been emphasized in ref. ^[11c], chemically exfoliated flakes have hydrophilic edges owing to facile deprotonation of terminating carboxyl groups in solution and largely hydrophobic basal planes due to the presence of polyaromatic domains of pure graphene^[13] (**Figure 1a**). The amphiphilicity of graphene oxide is a key factor responsible for segregation and formation of membranes at the liquid-air and liquid-solid interfaces in diluted solutions^[11c, 12, 14] and liquid crystal phases at high concentrations^[15]. Conveniently, the amphiphilic properties may be tuned by varying the solution pH, their size or via chemical reduction.^[11c] Moreover, it was demonstrated that as formed membranes are highly permeable to water due to capillary-driven intercalation between the overlapping micro flakes (Figure 1b) and yet impermeable to many other liquids, vapors, and gases including helium.^[12, 16] In a hydrated state a sharp cutoff in permeation of ions and molecules with hydration radius > 0.45 nm was observed^[16a]. Based on this peculiar selectivity of the membranes, a variety of applications, such as their use as ultrathin selective filters, have been proposed^[17]. Finally, the colloids are well suited for low cost and high yield aqueous processing, such as Langmuir–Blodgett, spin coating, nebulization, flow-directed assembly, jet printing, and drop casting protocols,^[11c] expanding the breadth of possible approaches for the graphene oxide-based encapsulation^[16a].

In the realm of biology, important demonstrations of graphene oxide flakes as deoxyribonucleic acid cargo or bio-sensing platforms for molecular probing in living cells have been also reported.^[18] Besides, protein-functionalized graphene has been successfully utilized to encapsulate live bacteria inside electron transparent cocoons suitable for *in vivo* transmission electron microscopy (TEM).^[19] The development of graphene oxide encapsulation of sulfur particles and metal oxide nanoparticles^[20] resulted in high energy density cathode composite materials for Li-ion batteries^[21]. In addition, aqueous solutions have been recently employed to encapsulate nanoparticles by aerosolizing suspensions followed by drying of micro-droplets,^[22] as well as used to create more effective matrices for mass spectroscopy^[23]. Finally, the effectiveness of graphene oxide colloids for toxic or radionuclide removal from solutions was demonstrated^[6b].

In this work, we concentrate on physicochemical details of GO membrane self-assembly in aqueous solution relevant to encapsulation, and adhesion of organic and inorganic micro-objects on planar and microstructured surfaces using drop-casting technique. We demonstrate the applicability of this technique to a wide class solid, liquid, and gaseous samples such as nanowires, nanoparticles, micro-droplets, bubbles, and microorganisms. We define the frames where scanning electron microscopy (SEM), scanning Auger microscopy (SAM), fluorescence and Raman spectroscopies can be successfully applied to image and analyze the encapsulated objects through the formed membrane.

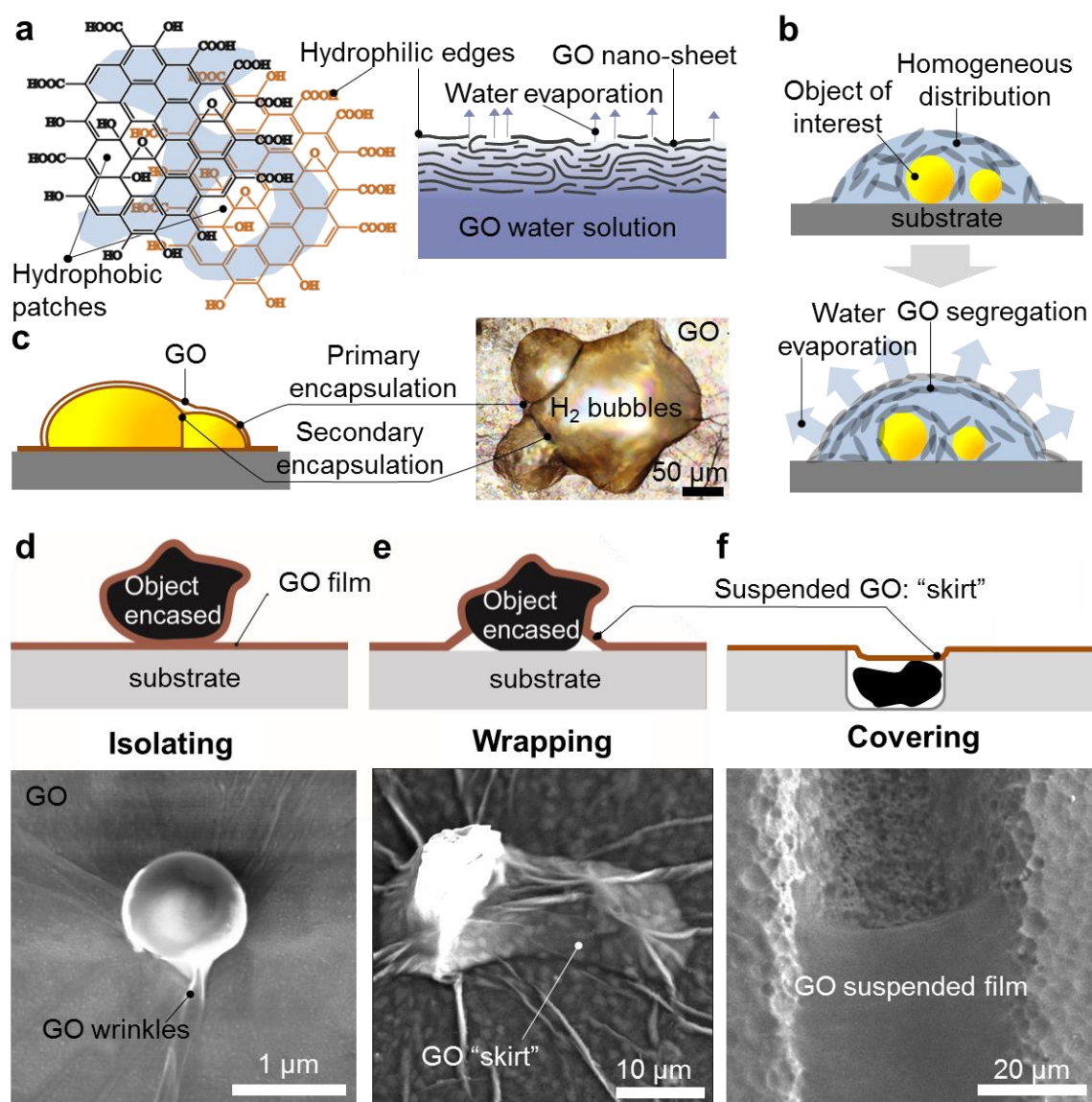


Figure 1. a) Two partially overlapping graphene oxide sheets (color coded) with hydrophilic end-groups and hydrophobic basal sites (left) and a schematic illustration of water intercalation and evaporation paths to the ambient in a membrane (right). b) Encapsulation steps: graphene oxide water solution drop cast on a sample followed by interfacial self-assembly of flakes, water intercalation and evaporation through the newly formed membrane. c) Drying of the membrane leads to primary and secondary encapsulation of micro-objects: an optical micrograph of encapsulated hydrogen bubbles. d) Three regimes of encasing: complete encapsulation of a polystyrene microparticle is manifested by the presence of a narrow “neck” connecting the objects to the surface. e) Wrapping of a SnO₂ microparticle: only top part of the object is in direct contact with the film. Empty “pockets” remain under the membrane along the perimeter of the sample. f) SEM of a trench in a glass substrate covered with the film.

2. Results and Discussion

The encapsulation of micro-objects via drop-casting of graphene oxide water solutions compatible with optical and high vacuum SEM (and SAM) studies has two related aspects: (i) the process of membrane formation around the object and (ii) its optical and electron imaging and spectroscopy through the membrane. Both of these aspects are discussed separately below to emphasize the effect of the encapsulation process on the samples final morphology as well as on the image formation and spectroscopic analysis.

2.1. Membrane Self-assembly and Encapsulation Process

The drying of colloids is an active field of research on its own,^[24] particularly for ultra-high aspect ratio discotic particles^[15a] and in relevance to the process of encapsulation. The latter proceeds generally via the following steps: (i) the membrane formation, (ii) solvent evaporation, and (iii) membrane drying. Once the diluted GO water solution is drop cast onto a nanoscopic or microscopic object on a substrate, the sample and the part of the substrate become submersed in homogeneous graphene oxide solution inside the droplet (Figure 1a). At low initial mass concentrations (w_{GO} from 0.05 g/g to 0.1 g/g), amphiphilic flakes with the average lateral size of a few to a few tens of micrometers slowly diffuse and segregate at all accessible liquid-gas, liquid-liquid or liquid-solid interfaces. During water evaporation, the concentration of graphene oxide inside the droplet and at interfaces steadily increases. As it has been shown,^[15] at concentrations exceeding $w_{GO} = 0.5$ g/g, the colloid experiences a transition from a disordered isotropic liquid phase to a self-assembled ordered phase similar to the one observed in nematic liquid crystals. This takes place predominately at the interfaces resulting in formation of lamella-like precursor membranes. On a molecular level, these precursor membranes consist of overlapping sheets with water filled percolating capillary network formed by polyaromatic domains. This network is responsible for facile unidirectional water transport from the interior of the droplet to the ambient^[12, 16b] (Figure 1b). As it has been shown recently, the interlocking between the flakes is greatly enhanced when traces of multivalent metal cations are present in the solution^[25]. The thickness of the nematic membrane increases until complete solvent evaporation, and the object becomes encapsulated. At the last stages of the membrane drying, the interlayer water evaporates, which is manifested by sudden changes in the optical properties and stress development in the membrane (see discussion below). Some amount of intercalated water remains inside of the membrane^[26] and can be desorbed only upon moderate (120 °C to 150 °C) annealing. As a result, the sample and surrounding substrate become covered with a robust laminate-like film, which has a nearly uniform thickness^[8b, 27]. This is quite opposite to the commonly observed “coffee-ring” effect in drying colloids^[28] and can be explained by a significant interaction between the 2D flakes and their hampered diffusion during the nematic phase of a drying droplet. Due to homogeneity and uniformity of the dried GO film, its final thickness h depends on the initial concentration C_{GO} (in kg/m³) of flakes in the solution and the cumulative area of covered surfaces S :

$$h \approx \frac{C_{GO} V_L}{S \rho_{GO}} \quad (1)$$

Here V_L and ρ_{GO} stand for initial volume of the graphene oxide droplet and final density of the dried membrane, respectively^[8b]. This approximation has experimentally proven effective for several values of GO dilution level and covered surface area^[8b].

The above scenario describes the membrane formation at the water-air interface and defines the so-called primary encapsulation. However, when the droplet contains multiple micro-objects with inner liquid-solid, liquid-liquid or liquid-gas interfaces, a secondary encapsulation may take place at those interfaces^[11c] (Figure 1b, c). To substantiate this point, an optically transparent objects can be used. For that, three hydrogen microbubbles were created inside the droplet by electrolysis. Figure 1c illustrates that both primary and secondary encapsulating membranes were formed at the air-graphene oxide solution and hydrogen bubble-solution interfaces, respectively.

Depending on the initial object and substrate topography, one can distinguish between three different encasing types: (i) when the solid sample has a small contact area with the substrate, the film encapsulates the item conformly (Figure 1d), and a complete “isolation” takes place. The complete isolation routinely occurs around solid grain-line objects or ones resting on hydrophobic surfaces where the interaction between the layer and the object dominates over the graphene oxide adhesion to the substrate. In the latter case, the drying membrane is capable of sliding over the substrate. Alternatively, when the solution wets the sample, the drying edge of the forming membrane becomes pinned to the substrate (Figure 1e).

This pinning front propagates from the periphery of the droplet toward the object upon drying, and the object becomes covered with the membrane having characteristic “skirt” around it (see SI movie). The formation of such a “skirt” implies that a partial interlocking between the individual flakes in the membrane takes place even before complete drying. Finally, when a solid object, gas bubble or water-immiscible liquid is confined inside a meso- (micro) pore or trench, the drying of the solution leads to the formation of a membrane, which covers the pore or trench (Figure 1f). The stability of the suspended membrane depends on the interplay between the capillary forces, the pressure differential (see below) and the mechanical stiffness of the membrane over the cavity. Figure 1f shows a trench partially covered with the membrane. Another example of a micro-well that was completely covered by a membrane is shown in Figure S1.

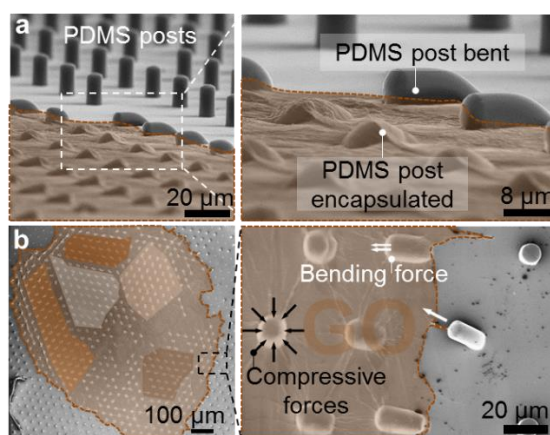


Figure 2. Interaction of a PDMS micro-post array with a membrane. a) side and b) top views of graphene oxide encapsulated (pseudo-colored) and pristine PDMS posts, respectively (SEM micrographs). Shadowed regions show different orientation of encapsulated micro-posts. Insets (right panels) depict the corresponding zoom-in regions.

Several effects that occur during the encapsulation process can strongly influence the final morphology of the encased objects. The main one is the buildup of the pressure differential between the ambient and encapsulated volume upon water evaporation. This pressure differential leads to contraction of the film around the object, complete wrapping around it and its deformation. There are two major origins of this effect. Firstly, a newly formed membrane is highly permeable to water molecules, and the solvent easily evaporates from the membrane covered droplet. On the other hand, the opposite diffusion of atmospheric gases is impeded. As a result, the residual gas pressure inside the shrinking encapsulated volume becomes reduced to saturated water vapor pressure ($\approx 3.2 \times 10^3$ Pa at room temperature) while the outside pressure is about 10^5 Pa. In fact, the unidirectional flux of water content acts as a vacuum pump on the encapsulated volume similar to a “vacuum storage bag” principle. Secondly, during the latest stages of encapsulation, a significant portion of water intercalated between graphene oxide stacks evaporates, leading to membrane’s appreciable shrinkage and an increase of its elastic modulus. The measurements of the membrane induced pressure differential showed that it does not exceed 10^5 Pa (see supporting material) in most of the encapsulating cases reported here. To visualize the forces acting on a sample and a substrate during drying of the solution, we monitored the encapsulation of an array of easily bendable polydimethylsiloxane (PDMS) micro-posts (**Figure 2**). The elastic properties of an individual PDMS post are well studied and allow one to detect bending and compressive forces as small as ≈ 1 nN^[29]. The typical strain maps (Figure 2) indicate the traction forces acting on samples located close to the edge of a drying drop due to initial pinning of the edge and shrinking of the membrane upon drying. Further away from the edge, the drying pattern becomes more symmetric, and compressive

forces affect the interior objects. The strain map, however, is not homogeneous on the millimeter scale but consists of a net of domains with different traction directions.

2.2. Encapsulation examples

The integrity of the encapsulating membrane as well as the resultant shape of the object strongly depend on the sample size, its mechanical properties, and graphene oxide adhesion to the substrate. Below, we provide several examples of encapsulation showing the applicability of this technique to a variety of objects of different nature.

We first tested nanoparticle opals^[30] as a model of a solid undeformable object for the encapsulation^[31]. A diluted solution of polystyrene nanoparticles (1 μm in diameter) was drop cast and dried on a cover glass pre-coated with Au film (**Figure 3a**). A typical formation of the opal structure with a characteristic “coffee-ring” effect was observed^[28]. After formation of a microparticle array, the graphene oxide-solution was drop cast on top. On drying, a typical wrapping topography of the membrane along with characteristic wrinkles and aforementioned peripheral “skirt” around the solid object is observed (Figure 3a). The membrane of the “skirt” is pinned to the object and the substrate and experiences about 10^5 Pa pressure differential. The tension applied to the object under the membrane is limited by the membrane’s tensile strength that can reach 120 MPa ^[11b] until it disrupts. As a result, a significant compression of the object under membrane can occur, promoting the close packing ordering of the microparticle array at the Au surface. A completely different encapsulation scenario was observed when nanoparticles and graphene oxide colloids were mixed together. The presence of immobile flakes in the nematic phase of the solution drastically impedes the mobility of the colloid microparticles inside the drying droplet. The result showed a strong suppression of the long range close pack ordering.

Graphene oxide encapsulation of immiscible liquids on a solid substrate represents another interesting class of practically important deformable objects^[31] demonstrating very different results as compared to encapsulated solid objects. As a model system, we used mercury that has poor wettability to most interfaces due to its high surface tension, leading to the well-known challenges in collecting toxic Hg spills. The contact angle between mercury and naturally oxidized aluminum is about 140° ^[32] resulting in an almost perfect spherical shape of a Hg drop on the substrate (Figure 3b). However, when the mercury drop is encapsulated, its shape becomes distorted with a significant reduction in the contact angle ($\approx 72^\circ$ in our case; Figure 3c). The mechanism behind this “wetting” behavior is depicted in the Figure 3e. As described in section 2.1, water surrounding the Hg droplet gradually evaporates through a permeable membrane. As a result, a membrane adheres to the substrate from edges toward the center until the film reaches the uppermost point of the Hg droplet (the central panel in the Figure 3e). At this moment, the liquid mercury starts deforming due to tension forces induced by the drying membrane and atmospheric pressure differential. Since the mercury drop is easily deformable, the initially spherical Hg droplet accepts a “pseudo-wetting” shape. Therefore, in contrast to the encapsulated solid items, deformable objects are able to mediate the pressure differential via changing their shapes during drying and without forming empty pockets (skirts). Note that this explanation implies strong membrane-substrate adhesion along the contact line of the membrane with naturally oxidized aluminum substrate. Therefore, the compression and shape of the encapsulated object can be controlled via tuning the membrane-substrate interaction. To validate this hypothesis, we reduced adhesion between the membrane and substrate by functionalizing the substrate with a hydrophobic coating (see methods section). The resulting shape of a Hg droplet became significantly less affected by the membrane in this case (Figure 3d) since the membrane is not pinned to the support anymore but slides over the hydrophobic surface. It results in conservation of nearly-spherical Hg droplet shape with a simultaneous increase in the number of wrinkles and thickness of the film that is in a good accordance with equation (1).

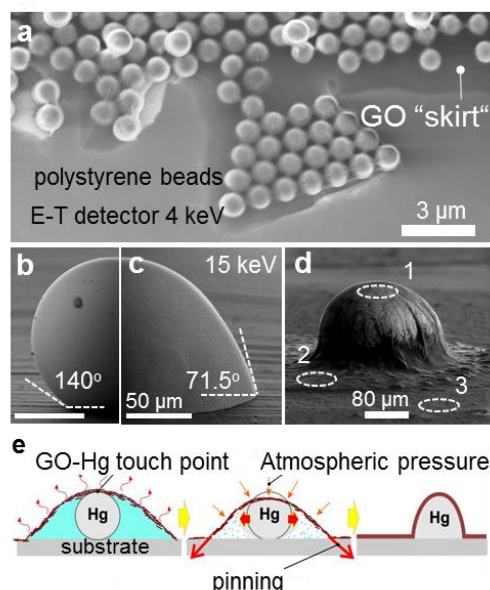


Figure 3. Graphene oxide encapsulation of polystyrene microparticles and mercury microdroplets as models of solid and liquid samples, respectively. a) An array of encapsulated ordered polystyrene microparticles. SEM images of b) uncovered and c) an encapsulated mercury microdroplet on an aluminum substrate acquired at $E_b=1$ keV and 15 keV, respectively. d) a Hg drop encapsulated on a chemically functionalized substrate at $E_b = 15$ keV. Regions encircled with white dashed contours correspond to collected spectra in Figure 7a. e) Graphene oxide-mercury interaction during encapsulation (from left to right): the film reaches and touches the top of Hg drop; Hg drop deforms due to the tension forces exerted on the film by atmospheric pressure; the film completely encapsulates the drop once water entirely evaporates.

Encapsulation of the biological objects is particularly important for histological and forensic applications. Graphene coating was previously used for non-destructive electron microscopy imaging and analysis of biological samples^[33]. Here, we apply graphene oxide encapsulation to exemplary biological objects and microorganisms such as pollen grains, *Daphnia*, and laboratory strains of *Escherichia coli* (*E. coli*) bacteria (**Figure 4**). The encapsulated grass pollen (Figure 4a) has a characteristic collapsed morphology, which is commonly observed during cellular dehydration. Graphene oxide encapsulation also enables reliable adhesion of the bio-samples to the substrate. According to our classification above (see Figure 1d), the observed encapsulation corresponds to a complete isolation since graphene oxide folds and wrinkles are distinctly seen at the very base of the pollen grain. Significantly larger hydrated organisms such as *Daphnia* experienced even higher degree of compression during the encapsulation. This is due to combined effect of dehydration and tension forces appearing in a drying membrane (Figure 4b). The morphological instabilities induced by the encapsulation can be seen as a drawback compared to standard CO₂ critical point drying technique. However, the advantage of the current method stems from the selective permeability of the membrane to water molecules. Therefore, the entire chemical content of the micro-object (except water) is preserved, which can be a decisive factor for forensic practices.

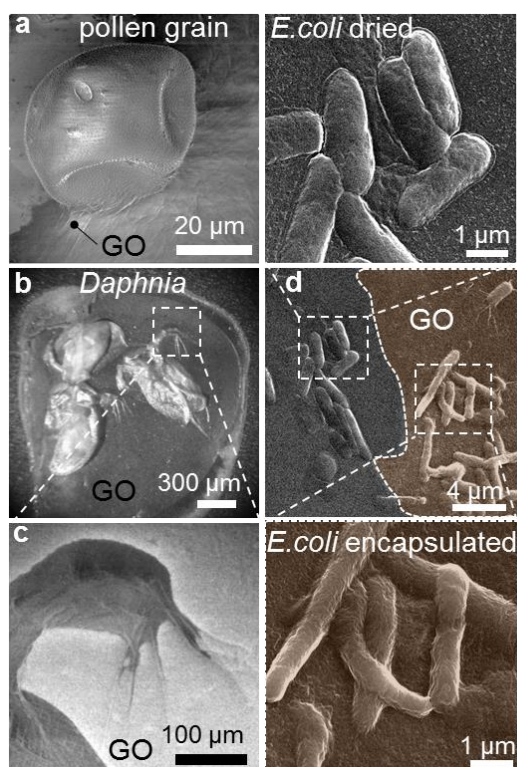


Figure 4. Encapsulated bio objects: a) a pollen grain, SEM at 1 keV; b) *Daphnia* (water flea) optical image; c) magnified SEM image (1 keV) of graphene oxide encapsulated antennae; d) Comparative SEM (10 keV) imaging of vacuum dried (top panel) and encapsulated (bottom panel) *E. coli* bacteria. The central panel represents the border between these two regions. Insets show the corresponding zoom-in regions. Encapsulated regions are shown in false color.

Other applications where an encapsulation can be essential, is isolation of pathogenic bacteria. This can be realized simply by spraying or spilling graphene oxide solution over the hazardous areas. To demonstrate the feasibility of this method, we have made side by side comparison of the areas containing untreated and encapsulated *E. coli* bacteria. The border region between the untreated and encapsulated bacteria was imaged with SEM (Figure 4d). A direct comparison of the pristine (Figure 4d left panel) and encapsulated (Figure 4d right panel) bacteria shows that the pristine samples do not preserve their shape and become flattened releasing their intracellular materials upon vacuum dehydration. On the other hand, the structure of the encapsulated bacteria is largely preserved by the membrane under the same conditions, thus preserving their initial content. In addition, it has been shown that the graphene oxide encapsulant not only immobilizes *E. coli* bacteria at the surface but also exhibits strong antibacterial activity^[34].

The last two encapsulation examples underline the role of the sample shape and size on the encapsulation scenario and membrane induced compression. Symmetric micro-objects such as bacteria, tend to be conformly coated with graphene oxide and, therefore, experience minor pressure differential mostly induced by membrane shrinkage upon drying. On the contrary, encapsulation of sub-millimeter samples with multiple protruding features (such as *Daphnia*) proceeds with creation of the numerous empty pockets under the membrane. The membrane experiences an additional tensile stress over these pockets which, in turn, leads to elevated compression.

2.3. Scanning Electron Imaging and Spectroscopy of graphene oxide encapsulated objects

There is a great interest in the development of encapsulation techniques, compatible with high-resolution microscopy and spectroscopy, which would not require traditional procedures such as fixation, staining, freezing or critical point drying. Unlike the common embedding media used in histology, the ultrathin graphene oxide film offers a unique possibility for imaging and probing the encased objects directly using the standard SEM (or TEM) without time-consuming microtoming, sectioning, and other histological procedures. The key advantage is that the membrane thickness can be tuned such that it becomes largely transparent to electrons in a wide range of electron beam energies. In this section we discuss the influence of the membranes on SEM signal attenuation as well as spatial resolution and comment on the optimal imaging conditions using several examples.

Following the traditional nomenclature (see for example ref.^[35]) primary electron (PE) beam generates low energy secondary electrons (SE) and higher energy backscattered electrons (BSE) upon inelastic and elastic collisions with graphene oxide coated sample.

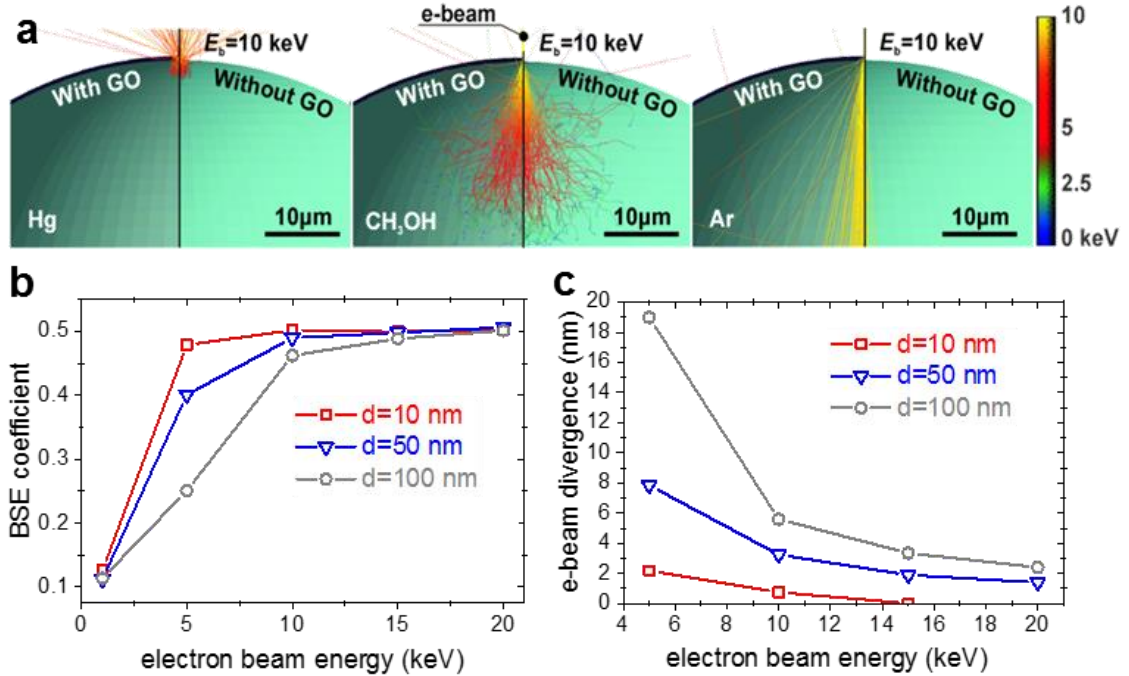


Figure 5. a) Monte Carlo simulations of electron scattering in liquid Hg drop of 13.5 g/cm³ density (left), liquid methanol of 0.79 g/cm³ density (center), and argon bubble of 1.7 · 10⁻³ g/cm³ density without the membrane (right-half of each panel) and encapsulated with a 50 nm thick graphene oxide film (left side of each panel). b) BSE coefficient vs. electron beam energy calculated for a Hg drop encapsulated with a 10 nm, 50 nm, and 100 nm thick film. c) Calculated divergence (in nm) of the electron-beam scattered by 10 nm, 50 nm, and 100 nm thick film as a function of primary electron energy.

To evaluate the influence of the coating on SEM imaging, we conducted comparative Monte Carlo (MC) trajectory simulations^[36] for 10 keV electron beam probing: (i) high atomic number (Z) metal (Hg, 201 u), (ii) liquid droplet (CH₃OH, 32 u), and (iii) gas (10⁵ Pa Ar, 40 u) bubbles with and without a 50 nm thick graphene oxide coverage (**Figure 5a**). The interaction volumes at 10 keV electron beam energy for the aforementioned materials covered with a membrane and without coverage are depicted at the left and right halves of each panel, respectively. The parametric Kanaya-Okayama expression for electron beam range^[35] $R_{KO} \approx 0.0276A \cdot E^{1.67} / Z^{0.89} \cdot \rho$ predicts $R_{KO} = 0.38 \mu\text{m}$ and $R_{KO} = 9 \mu\text{m}$ for Hg and methanol droplets, respectively; here A is the molar mass [g/mol], E is the primary electron beam energy [keV], and ρ is the material's density [g/cm³]. As can be seen, a 50 nm thick membrane does not profoundly affect the interaction

volume in mercury and methanol and it is primarily due to low scattering of electrons in graphene oxide and much higher Z number of the host materials. The contribution of the membrane to electron scattering becomes, however, dominating in the case of gaseous samples (Figure 5a, right panel) due to a three orders of magnitude reduction in the density compared to solid or liquid encapsulated sample.

Figure 5b depicts the variation of the BSE coefficient (the number of elastically scattered BSEs electrons per primary electron) of a graphene oxide covered Hg droplet as a function of electron beam energy for three different thicknesses of the membrane. The BSE coefficient is relatively small for the 50 nm and 100 nm thick coatings and the interaction volume is mostly confined within the shell when the primary electron energy E_b is low. Under these conditions, the image mainly contains surface topographical information. With E_b increase, the interaction volume increases with a dominant contribution to BSE coefficient from the core material. Contrarily, relatively thin film, e.g. 10 nm, is highly transparent to primary electron beam at 5 keV electron energy, thus, BSE is dominated by the high Z Hg encapsulated interior. In summary, for electron beam energies of 10 keV and above, the BSE coefficient is nearly independent of the membrane thickness if it is less than 100 nm. At lower electron energies, the attenuation of the BSE signal by the membrane becomes noticeable and strongly depends on the film thickness. The latter may be used to image the completeness of the coverage of high Z materials. Figure 5c shows the calculated divergence of 10 nm wide primary electron beam propagating in a gaseous medium after passing the membranes at three different thicknesses. The cross-sectional region containing 68 % of transmitted electrons was used as an effective beam diameter.^[37] Apparently, the divergence of the beam grows with increase of the film thickness and reduction of primary electron energy, affecting the ultimate resolution achievable on the encapsulated objects.

To experimentally validate the simulated results, we imaged the coated SnO₂ whiskers and hydrogen bubbles at different SEM settings. **Figure 6a** and **b** show two images of the same area recorded using surface sensitive and bulk sensitive imaging conditions, respectively. Under these conditions, low-energy e-beam and a secondary electron sensitive through-the-lens (TTL) detector reveal mostly the surface topography of the film covering the SnO₂ sample (Figure 6a) while the high-energy e-beam in conjunction with the BSE detector probes the interior of the encased object through the membrane (Figure 6b). High electron transparency of the graphene oxide coating to the outgoing backscattered electrons enables detection of even small diameter SnO₂ nanowires (Figure 6b) that were completely invisible beneath the membrane (Figure 6a) when lower electron energies were used.

Gaseous samples provide an ideal platform to quantify the attenuation and scattering of the electron beam during SEM imaging of the encapsulated objects. For that, a microchannel plate (MCP) was used as a substrate with sharp topographical features and high secondary electron yield surface suitable for resolution tests. A graphene oxide solution was drop cast onto MCP microporous surface followed by oxygen or hydrogen bubbles generation beneath the membrane. In agreement with prior MC simulations, Figure 6 c-f demonstrates a gradual decrease of electron scattering by the thin encapsulating membrane resulting in an increase of electron transparency of the membrane and lateral resolution of the underlying substrate with electron energy.

Besides SEM imaging, graphene oxide electron transparent films open exciting avenues for spectroscopic analysis of encapsulated samples. **Figure 7a** shows EDS spectra taken at different locations: (1) on a Hg drop covered with the membrane, (2) Al substrate covered with the same film, and (3) pristine Al substrate (see Figure 3 for details). Despite a thick membrane, these spectra demonstrate the feasibility of EDS elemental analysis of encapsulated objects. In a different experiment, differential Auger spectra (AES) were acquired comparatively from two adjacent graphene oxide-covered (blue curve) and uncovered (red curve) areas of a SnO₂ whisker (Figure 7b). As expected, the carbon C_{KVV} Auger peak dominates the spectrum from

the covered area, however, a strongly attenuated tin Sn_{MNN} signal can still be recorded. This result is somewhat surprising since the average thickness of the membrane is expected to be more than 10 nm based on the concentration of the solution and the droplet size.

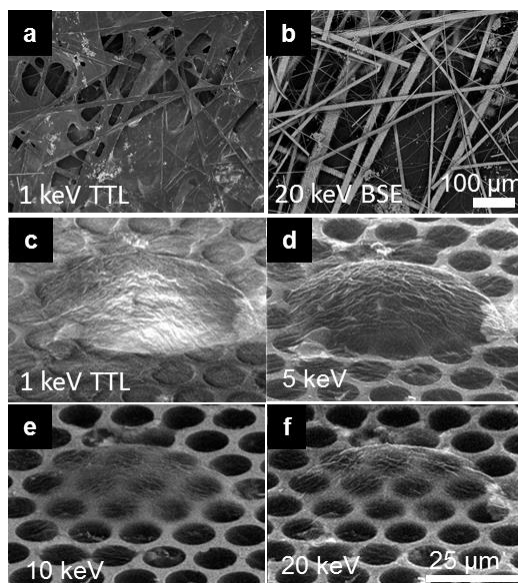


Figure 6. Electron transparency of graphene oxide membrane and e-beam divergence. a) SEM image of encapsulated SnO_2 whiskers obtained using secondary electron sensitive TTL detector and low energy electron beam $E_b = 1$ keV. b) The same object imaged using BSE detector and $E_b = 20$ keV. c)-f) The evolution of membrane transparency with electron beam energy via imaging of the same encapsulated H_2 bubble at $E_b = 1$ keV, 5 keV, 10 keV, and 20 keV.

The standard attenuation equation^[38]:

$$I_{\text{Sn}}/I_{\text{Sn}}^0 = \exp(-d/\lambda_{\text{MNN}} \cdot \cos \varphi), \quad (2)$$

where d is the thickness of the graphene oxide layer, λ_{MNN} is Sn_{MNN} electron attenuation length in graphene oxide layer, and φ is the take-off angle (25°), allows estimating the thickness of the membrane via given peak-to-peak intensity ratio of the Auger Sn_{MNN} signal from pristine and covered areas. The recorded ratio corresponds to the thickness of just one or two monolayers. The observed discrepancy requires further investigation and is presumably a result of electron beam induced chemical reduction of the membrane under intense irradiation^[39]. Despite the possible graphene oxide electron beam induced local decomposition, the spectra demonstrate the possibility to obtain fine chemical information for analytical purposes from an encapsulated object using standard electron spectroscopy.

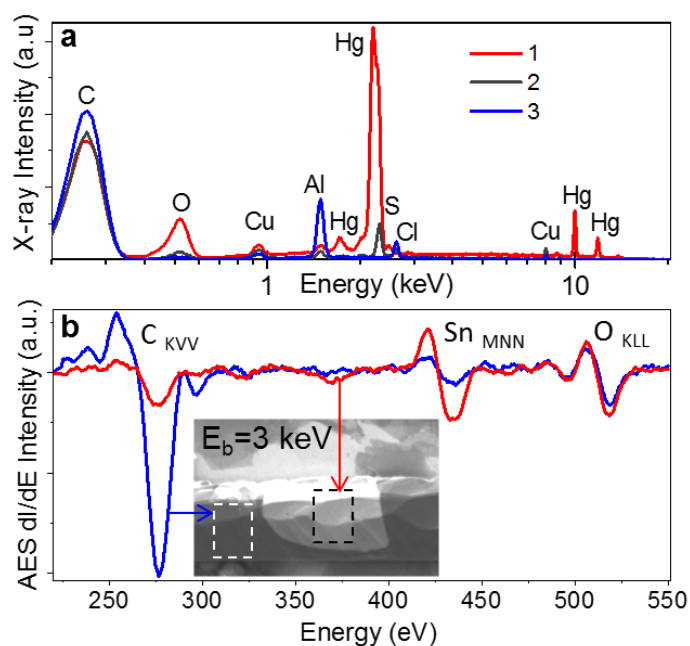


Figure 7. Electron spectroscopy through a thin graphene oxide membrane. a) EDS spectra marked as 1, 2, and 3 are collected from graphene oxide encapsulated Hg microdroplet ($E_b=15$ keV), Al substrate covered with graphene oxide film, and Al substrate shown in Figure 3d, respectively. Al, C, and O peaks originate from Al substrate. b) Differential Auger spectra ($E_{PE}=3$ keV) collected from pristine SnO_2 (red curve) and covered areas (blue curve).

2.4. Optical transparency and Raman spectroscopy

Optical microscopy and spectroscopy are major tools for materials science, forensics, and biomedical research. Transparency of thin-film graphene oxide membranes not only to electrons but also to optical photons enables facile fluorescence and Raman analysis of the encapsulated materials. To demonstrate this, we used fluorescent polystyrene microparticles which are common in drug discovery, phagocytosis, and microfluidic studies and serve as good model objects for encapsulation tests. **Figure 8a** and **b** show images of the same area containing fluorescent microparticle deposit recorded using an optical microscope operating either in the bright field or fluorescence imaging modes. A white dashed line in the Figure 8b demarks the border between the encapsulated and pristine arrays of particles. In contrast to prior observations^[40] where graphene oxide was used to quench surface fluorescence, only a minor attenuation of the fluorescence signal from microparticles was observed in our experiments. This is due to the high optical transparency of the membrane for the 480 nm to 550 nm emission band^[41] and the bulk doping of polystyrene microparticles with a dye.

An example of Raman spectroscopy through a membrane is shown in Figure 8c. Here, a grain of crystalline naphthalene was encapsulated with graphene oxide in an attempt to preserve this highly volatile material. The stability and comparative analysis of the sublimation rates for pristine and encapsulated naphthalene is an interesting problem of its own, which remains beyond the scope of this work. The recorded spectrum is a superposition of sharp peaks corresponding to the Raman signatures of naphthalene (red curve) and broad characteristic graphene oxide peaks (blue curve). Due to the small thickness, the contribution of the membrane to the cumulative Raman signal is insignificant compared to naphthalene. This experiment exemplifies the feasibility of high-quality Raman analysis through the

encapsulating membrane. The latter opens exciting opportunities for analytic forensic applications where preservation of probed materials is required.

3. Outlook and conclusions

In conclusion, we have demonstrated that a wide class of solid, liquid, gaseous micro- and mesoscopic objects can be reliably adhered to a variety of substrates and encapsulated with an electron (and optically) transparent membranes using a simple drop casting method. The thickness of the membrane can be tuned by the concentration of the solutions and the size of the droplet. Different regimes of encapsulation such as covering, wrapping, and complete isolation of objects can be realized depending on the hydrophobicity and/or topography of a substrate surface. The shape and morphology of encapsulated objects may change upon encapsulation due to pressure differential buildup and membrane shrinkage. This effect is particularly noticeable in the case of soft, deformable, and biological samples.

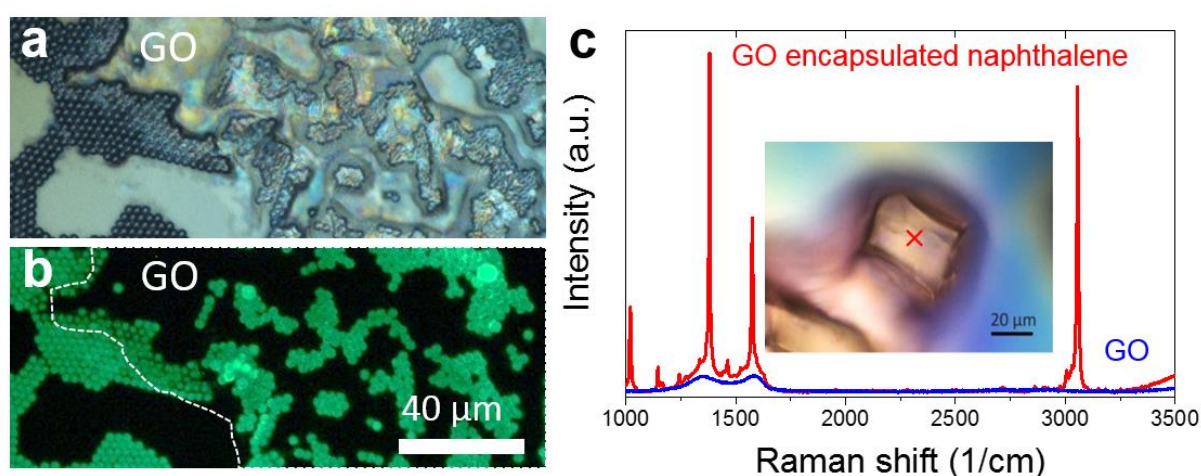


Figure 8. a) The bright field and b) fluorescence microscopy images of an array of fluorescent 4 μm in diameter polystyrene microparticles partly encapsulated with graphene oxide. The white dashed line demarcates the border between the pristine and covered microparticles. c) Raman spectra of a covered naphthalene grain (red) and pristine graphene oxide film (blue). The Raman signal from naphthalene was collected through an optically transparent film. The cross in the inset image shows the location where the data were collected.

Due to the low atomic number of carbon and small thickness of the film, it is largely transparent to photons and even to a few keV electrons enabling routine fluorescence, Raman, X-ray, SEM, scanning TEM (STEM) imaging, and chemical analysis (EDS, AES) of encapsulated micro-objects through a membrane. Though few monolayer thin membranes can be fabricated, a 50 nm to 200 nm range of the film thickness defines a practical compromise between its mechanical strength and electron transparency in the 5 keV to 30 keV electron energy range. Tight adhesion between the membrane and the sample minimizes electron attenuation and broadening effects in the membrane.

Graphene oxide encapsulation can find an application as a new protocol in histology. As an example, the conventional sample preparation for TEM and STEM imaging relies on van der Waals adhesion of the sample to electron transparent supporting membranes or special TEM grids. Alternatively the samples are often glued or embedded into a polymerized resin block followed by microtoming^[5]. However, due to either poor adhesion or incompatibility with glues, resins, toxicity, etc., a large class of samples cannot be easily prepared using aforementioned recipes. Our approach provides a complementing way to snugly attach an arbitrary micro sample to membranes and stencils with a precise control of the film thickness. **Figure 9a** shows an STEM image of *E. coli* bacteria on a 50 nm thick polyimide TEM grid encapsulated by

graphene oxide (right panel) and uncovered (left panel). The central image comprises both encapsulated and non-encapsulated regions^[31]. Figure 9d exemplifies our approach to fix and image a grass pollen in STEM mode. The symmetrical radial wrinkles visible in a transmission mode prove a complete encapsulation of the pollen on a very thin TEM membrane.

Another potentially important application of this encapsulation technique is X-ray micro-tomography. Usually, to obtain a 3D reconstruction of an object, a set of 2D images of the sample pivoted within a wide range of angles $\pm 70^\circ$ is recorded^[42]. This technique requires mounting the sample on a pivoting axis with an open access for the X-rays in the aforementioned angle range. Currently, the latter raises design challenges in sample mounting. Our approach helps resolve many of impediments via attaching a micro sample to the needle-like holder and encapsulating an object of interest by graphene oxide (Figure 9c). Here, an X-ray transparent graphene oxide film serves as both supporting media for the micro sample and the isolation membrane from the ambient environment (when necessary).

Finally, along with the benefits in performing routine optical, X-ray, and SEM/STEM imaging and analysis, the elemental composition of membranes is favorable for other analytical methods such as flame photometry, mass-spectroscopy methods i.e. matrix-assisted laser desorption/ionization (MALDI). This is due to the fact that destruction of the membrane during analysis leads to simple and easily identifiable molecules such as CO and CO₂. We envision that scalable, inexpensive, and high-yield graphene oxide encapsulation will open new routes in histological practices, forensic studies, dip pen-like encapsulation technology and other fields where reliable adhesion and isolation of reactive, toxic/radioactive samples or precious artifacts is required. Furthermore, the technique can be easily integrated with the modern microelectronic and microfluidic methods and applications.

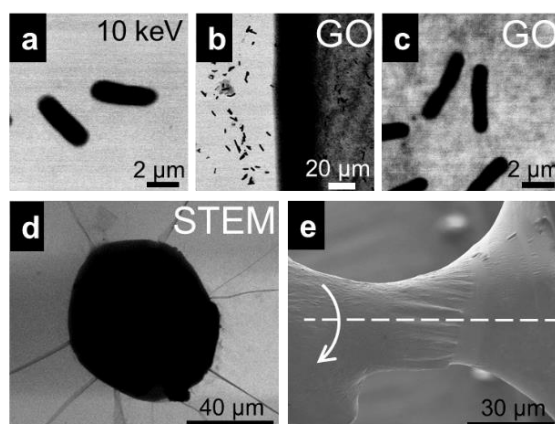


Figure 9. *E. coli* bacteria and a pollen grain encapsulated by graphene oxide on a TEM membrane and sample preparation for X-ray microtomography and 3D imaging. Comparative STEM (10 keV) imaging of vacuum dried (a) and left part of (b) and encapsulated (c) and right panel of (b) *E. coli* bacteria. d) A pollen grain imaged in STEM mode at $E_b=20$ keV. e) Liquid Ga neck formed between the needle and a solid surface and wrapped with the membrane. Part of the membrane was torn away (right side) exposing the surface of pristine Ga. The dashed line represents the axis of rotation.

4. Experimental

Samples preparation: Graphene oxide solution was fabricated according to standard Hummers method followed by dispersing in water via sonication to obtain homogeneous suspension^[11b, 12, 43]. Different concentrations of the solution ($0.02 \text{ kg/m}^3 - 1 \text{ kg/m}^3$) were used to tune the thickness of the drop-cast membranes. SiO₂/Si wafers and different metal substrates were employed as solid supports for objects of interest. To study the effect of wetting on encapsulation dynamics, the surface was functionalized with a hydrophobic silane. Besides planar substrates, microchannel arrays made of a boron doped silicate glass were used.

Hydrogen bubbles were produced in graphene oxide water solution by electrolysis. A water drop was placed on top of two copper electrodes, and a DC electrolysis was initiated. PDMS microparticles were synthesized using microfluidic setup^[44]. PDMS micro-posts were created using standard photolithography base approach to fabricate elastomeric stamps for soft lithography. Water fleas (*Daphnia*) were transferred on a Si substrate with micropipette from culture liquid. The laboratory strain of *E-coli* bacteria and grass pollen followed a similar encapsulation by drop casting procedure. All experiments involving biological samples: *Daphnia*, *E-coli* bacteria, and grass pollen were conducted at the SIUC campus.

Imaging: An optical microscope and field emission SEM were employed to observe the encapsulation process and final products. The electron beam energy and type of an electron detector were varied to gain the desired contrast of encapsulated objects. Electron trajectory simulations were calculated by means of Monte Carlo simulation package^[36]. For scanning transmission electron microscopy (STEM) specimens were placed onto a 50 nm thick polyimide TEM grid. The latter was mounted on a carbon STEM holder with Au covered plate facing E-T detector. Electrons transmitted through the sample produced the image formed by a secondary electron signal scattered from the gold surface. Therefore, the image could be created concurrently by either conventional SE₁ scattered from the specimen and collected by TTL detector or by transmitted signal resulting in SE₂ and analyzed by E-T detector. Atomic force microscopy (AFM) images were obtained in a tapping mode at a scan rate of 0.5 Hz.

Raman spectroscopy:

The Raman spectra were collected using a Raman microscope with a 532 nm excitation laser. Laser power was set to 2 mW. We used 25 μm slit aperture and 50 \times objective. The estimated spot size was 2.1 μm .

Auger spectroscopy:

For Auger spectroscopy the samples were admitted to an UHV analytical chamber using standard load-lock system. No additional cleaning or baking procedures were undertaken. Auger electrons were excited by a 3 keV primary e-beam and collected at takeoff angle close to normal to the sample surface. Hemispherical electron energy analyzer was set to 100 eV pass energy.

Acknowledgements

The authors are thankful to Prof. J. Huang (Northwestern University) and Dr. N. Kovtyukhova (Penn State University) for fruitful discussions and graphene oxide samples; Prof. S. R. Raghavan (UMD), Drs. V. Szalai and Y. Lee (NIST) for their help with PDMS beads and micro-post arrays. We appreciate Prof. V. Konjufca and Prof. M. Brooks (both at SIUC) help with preparation and handling of biological samples. This work has been supported in part by the NIST-CNST/UMD-IREAP Cooperative Agreement. A. L. and A. S. acknowledge a partial support from the National Science Foundation (NSF) through the Nebraska Materials Research Science and Engineering Center (MRSEC) (grant no. DMR-1420645).

References

- [1] a) A. G. Aberle, *Progress in Photovoltaics: Research and Applications* **2000**, 8, 473; b) P. M. Wilson, A. Zobel, A. Lipatov, E. Schubert, T. Hofmann, A. Sinitskii, *ACS applied materials & interfaces* **2015**, 7, 2987.
- [2] R. H. Muller, K. Mader, S. Gohla, *European Journal of Pharmaceutics and Biopharmaceutics* **2000**, 50, 161.
- [3] a) B. Sobrino, M. Brion, A. Carracedo, *Forensic science international* **2005**, 154, 181; b) R. Saferstein, *Criminalistics. Prentice Hall, Upper Saddle River, New Jersey* **2001**, 108.
- [4] a) B. Herrmann, S. Hummel, *Ancient DNA: recovery and analysis of genetic materials from paleontological, archeological, museum, medical, and forensic specimens.*, Springer Verlag, **1994**; b) M. T. Gonzalez-Arno, F. Engelmann, *CryoLetters* **2006**, 27, 155.
- [5] J. J. Bozzola, L. D. Russell, *Electron microscopy: principles and techniques for biologists*, Jones & Bartlett Learning, **1999**.
- [6] a) C. Grupen, *Introduction to radiation protection: practical knowledge for handling radioactive sources*, Springer, **2010**; b) A. Y. Romanchuk, A. S. Slesarev, S. N. Kalmykov, D. V. Kosynkin, J. M. Tour, *PCCP* **2013**, 15, 2321.
- [7] J. L. Wierman, J. S. Alden, C. U. Kim, P. L. McEuen, S. M. Gruner, *J. Appl. Crystallogr.* **2013**, 46, 1501.
- [8] a) A. Kolmakov, D. A. Dikin, L. J. Cote, J. Huang, M. K. Abyaneh, M. Amati, L. Gregoratti, S. Gunther, M. Kiskinova, *Nature Nanotechnology* **2011**, 6, 651; b) M. Krueger, S. Berg, D. A. Stone, E. Strelcov, D. A. Dikin, J. Kim, L. J. Cote, J. Huang, A. Kolmakov, *ACS nano* **2011**, 5, 10047; c) J. M. Yuk, J. Park, P. Ercius, K. Kim, D. J. Hellebusch, M. F. Crommie, J. Y. Lee, A. Zettl, A. P. Alivisatos, *Science* **2012**, 336, 61.
- [9] a) Y. Zhu, S. Murali, W. Cai, X. Li, J. W. Suk, J. R. Potts, R. S. Ruoff, *Adv. Mater.* **2010**, 22, 3906; b) D. Li, M. B. Muller, S. Gilje, R. B. Kaner, G. G. Wallace, *Nature Nanotechnology* **2008**, 3, 101.
- [10] a) N. R. Wilson, P. A. Pandey, R. Beanland, R. J. Young, I. A. Kinloch, L. Gong, Z. Liu, K. Suenaga, J. P. Rourke, S. J. York, *ACS nano* **2009**, 3, 2547; b) J. C. Meyer, C. O. Girit, M. Crommie, A. Zettl, *Nature* **2008**, 454, 319.
- [11] a) N. Kovtyukhova, E. Buzaneva, A. Gorchinsky, P. Ollivier, B. Martin, C. Waraksa, T. Mallouk, in *Frontiers of Nano-Optoelectronic Systems*, Springer, 2000, 331; b) D. A. Dikin, S. Stankovich, E. J. Zimney, R. D. Piner, G. H. B. Dommett, G. Evmenenko, S. B. T. Nguyen, R. S. Ruoff, *Nature* **2007**, 448, 457; c) J. Kim, L. J. Cote, F. Kim, W. Yuan, K. R. Shull, J. Huang, *JACS* **2010**, 132, 8180; d) C. Chen, Q.-H. Yang, Y. Yang, W. Lv, Y. Wen, P.-X. Hou, M. Wang, H. M. Cheng, *Advanced Materials* **2009**, 21, 3007.
- [12] R. Nair, H. Wu, P. Jayaram, I. Grigorieva, A. Geim, *Science* **2012**, 335, 442.
- [13] K. Erickson, R. Erni, Z. Lee, N. Alem, W. Gannett, A. Zettl, *Adv. Mater.* **2010**, 22, 4467.
- [14] W. Lv, Z. Xia, S. Wu, Y. Tao, F. M. Jin, B. Li, H. Du, Z. P. Zhu, Q. H. Yang, F. Kang, *J. Mater. Chem.* **2011**, 21, 3359.
- [15] a) B. Dan, N. Behabtu, A. Martinez, J. S. Evans, D. V. Kosynkin, J. M. Tour, M. Pasquali, I. I. Smalyukh, *Soft Matter* **2011**, 7, 11154; b) J. E. Kim, T. H. Han, S. H. Lee, J. Y. Kim, C. W. Ahn, J. M. Yun, S. O. Kim, *Angew. Chem. Int. Ed.* **2011**, 50, 3043; c) Z. Xu, C. Gao, *ACS nano* **2011**, 5, 2908; d) F. Guo, F. Kim, T. H. Han, V. B. Shenoy, J. Huang, R. H. Hurt, *ACS nano* **2011**, 5, 8019.
- [16] a) R. Joshi, P. Carbone, F. Wang, V. Kravets, Y. Su, I. Grigorieva, H. Wu, A. Geim, R. Nair, *Science* **2014**, 343, 752; b) D. W. Boukhvalov, M. I. Katsnelson, Y.-W. Son, *Nano Lett.* **2013**, 13, 3930; c) A. V. Talyzin, T. Hausmaninger, S. You, T. Szabó, *Nanoscale* **2014**, 6, 272.
- [17] a) H. Li, Z. Song, X. Zhang, Y. Huang, S. Li, Y. Mao, H. J. Ploehn, Y. Bao, M. Yu, *Science* **2013**, 342, 95; b) H. W. Kim, H. W. Yoon, S.-M. Yoon, B. M. Yoo, B. K. Ahn, Y. H. Cho, H. J. Shin, H. Yang, U. Paik, S. Kwon, *Science* **2013**, 342, 91; c) M. Hu, B. Mi, *Environmental science & technology* **2013**, 47, 3715; d) K. Raidongia, J. Huang, *JACS* **2012**, 134, 16528.

- [18] Y. Wang, Z. Li, D. Hu, C. T. Lin, J. Li, Y. Lin, *JACS* **2010**, 132, 9274.
- [19] N. Mohanty, M. Fahrenholtz, A. Nagaraja, D. Boyle, V. Berry, *Nano Lett.* **2011**, 11, 1270.
- [20] D. Wei, J. Liang, Y. Zhu, Z. Yuan, N. Li, Y. Qian, *Particle & Particle Systems Characterization* **2013**, 30, 143.
- [21] a) H. Wang, Y. Yang, Y. Liang, J. T. Robinson, Y. Li, A. Jackson, Y. Cui, H. Dai, *Nano Lett.* **2011**, 11, 2644; b) G. Zhou, D.-W. Wang, F. Li, L. Zhang, N. Li, Z.-S. Wu, L. Wen, G. Q. Lu, H.-M. Cheng, *Chem. Mater.* **2010**, 22, 5306.
- [22] a) Y. Chen, F. Guo, A. Jachak, S.-P. Kim, D. Datta, J. Liu, I. Kulaots, C. Vaslet, H. D. Jang, J. Huang, *Nano Lett.* **2012**, 12, 1996; b) J. Luo, X. Zhao, J. Wu, H. D. Jang, H. H. Kung, J. Huang, *The Journal of Physical Chemistry Letters* **2012**, 3, 1824.
- [23] Q. Liu, J. Shi, M. Cheng, G. Li, D. Cao, G. Jiang, *Chem. Commun.* **2012**, 48, 1874.
- [24] A. F. Routh, *Rep. Prog. Phys.* **2013**, 76, 046603.
- [25] C.-N. Yeh, K. Raidongia, J. Shao, Q.-H. Yang, J. Huang, *Nature chemistry* **2015**, 7, 166.
- [26] M. Acik, C. Mattevi, C. Gong, G. Lee, K. Cho, M. Chhowalla, Y. J. Chabal, *ACS nano* **2010**, 4, 5861.
- [27] P. J. Yunker, T. Still, M. A. Lohr, A. Yodh, *Nature* **2011**, 476, 308.
- [28] R. D. Deegan, O. Bakajin, T. F. Dupont, G. Huber, S. R. Nagel, T. A. Witten, *Nature* **1997**, 389, 827.
- [29] a) J. L. Tan, J. Tien, D. M. Pirone, D. S. Gray, K. Bhadriraju, C. S. Chen, *Proceedings of the National Academy of Sciences* **2003**, 100, 1484; b) Q. Cheng, Z. Sun, G. Meininger, M. Almasri, *une* **2016**, 13, 15.
- [30] Y. Ma, H. Davis, L. Scriven, *Progress in Organic Coatings* **2005**, 52, 46.
- [31] A. Yulaev, A. Lipatov, A. Sinitskii, A. Kolmakov, *Microsc. Microanal.* **2014**, 20, 1798.
- [32] O. D. Neikov, S. S. Naboychenko, *Handbook of non-ferrous metal powders: technologies and applications*, Elsevier Science Limited, **2009**.
- [33] a) J. B. Park, Y.-J. Kim, J. M. Yoo, Y. Kim, S.-M. Kim, S. J. Kim, R. Gorbachev, I. Barbolina, M.-H. Yoon, B. H. Hong, K. S. Novoselov, *arXiv preprint arXiv:1407.2070* **2014**; b) M. Wojcik, M. Hauser, W. Li, S. Moon, K. Xu, *Nature communications* **2015**, 6, 7384; c) J. Park, H. Park, P. Ercius, A. F. Pegoraro, C. Xu, J. W. Kim, S. H. Han, D. A. Weitz, *Nano Lett.* **2015**, 15, 4737; d) R. Kempaiah, S. Salgado, W. L. Chung, V. Maheshwari, *Chem. Commun.* **2011**, 47, 11480.
- [34] S. Liu, M. Hu, T. H. Zeng, R. Wu, R. Jiang, J. Wei, L. Wang, J. Kong, Y. Chen, *Langmuir* **2012**, 28, 12364.
- [35] J. Goldstein, D. E. Newbury, D. C. Joy, C. E. Lyman, P. Echlin, E. Lifshin, L. Sawyer, J. R. Michael, *Scanning electron microscopy and X-ray microanalysis*, Springer, **2003**.
- [36] H. Demers, N. Poirier-Demers, A. R. Couture, D. Joly, M. Guilmain, N. de Jonge, D. Drouin, *Scanning* **2011**, 33, 135.
- [37] S. Thiberge, O. Zik, E. Moses, *Rev. Sci. Instrum.* **2004**, 75, 2280.
- [38] S. Hofmann, *Surface and Interface Analysis* **1980**, 2, 148.
- [39] M. Xu, D. Fujita, N. Hanagata, *Nanotechnology* **2010**, 21, 265705.
- [40] J. Kim, L. J. Cote, F. Kim, J. Huang, *JACS* **2009**, 132, 260.
- [41] G. Eda, G. Fanchini, M. Chhowalla, *Nature nanotechnology* **2008**, 3, 270.
- [42] a) P. J. Withers, *Materials today* **2007**, 10, 26; b) P. A. Midgley, E. P. Ward, A. B. HungrÅ-a, J. M. Thomas, *Chemical Society Reviews* **2007**, 36, 1477; c) A. Hitchcock, J. Wang, M. Obst, *Microscopy and Microanalysis* **2010**, 16, 850.
- [43] a) W. S. Hummers Jr, R. E. Offeman, *JACS* **1958**, 80, 1339; b) N. I. Kovtyukhova, P. J. Ollivier, B. R. Martin, T. E. Mallouk, S. A. Chizhik, E. V. Buzaneva, A. D. Gorchinskiy, *Chem. Mater.* **1999**, 11, 771.
- [44] K. Jiang, P. C. Thomas, S. P. Forry, D. L. DeVoe, S. R. Raghavan, *Soft Matter* **2012**, 8, 923.

Supporting Information should be included here (for submission only; for publication, please provide Supporting Information as a separate PDF file).

Supporting material for

Imaging and Analysis of Encapsulated Objects through Electron and Optically Transparent Graphene Oxide Membranes

Alexander Yulaev^{1,2,3}, Alexey Lipatov⁴, Annie Xi Lu⁵, Alexander Sinitskii^{4,6}, Marina S. Leite^{1,7}
and Andrei Kolmakov^{3*},

¹ Department of Materials Science and Engineering, University of Maryland, College Park, MD 20742 USA

² Maryland NanoCenter, University of Maryland, College Park, MD 20742, USA

³ Center for Nanoscale Science and Technology at NIST, 100 Bureau Drive, Gaithersburg, MD 20899-6204 USA

⁴ Department of Chemistry, University of Nebraska – Lincoln, Lincoln, NE 68588, USA

⁵ Department of Chemical & Biomolecular Engineering University of Maryland, College Park, MD 20742-2111

⁶ Nebraska Center for Materials and Nanoscience, University of Nebraska – Lincoln, Lincoln, NE 68588, USA

⁷ Institute for Research in Electronics and Applied Physics, University of Maryland, College Park, MD 20742, USA

E-mail: andrei.kolmakov@nist.gov

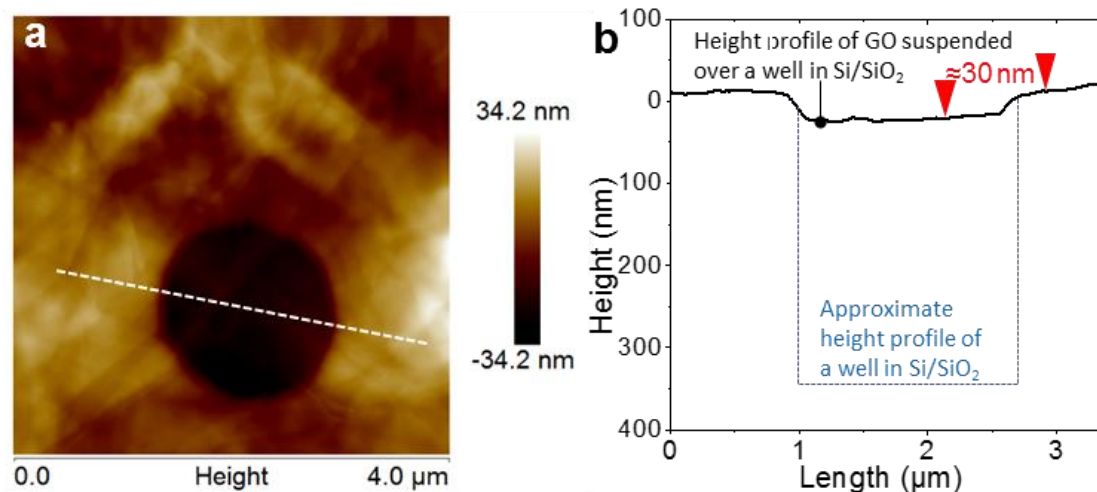


Figure S1. A microwell in Si/SiO₂ that is fully covered by a graphene oxide membrane. The well, that is ≈ 1.5 μm in diameter and ≈ 350 nm deep, was created by electron-beam lithography and reactive ion etching. Then, a droplet of a graphene oxide aqueous solution was drop-cast on the substrate and dried in air. a) A projection of an AFM image of a covered microwell. b) Height profile of graphene oxide suspended over a microwell measured along the white line in (a). The vertical distance between the red triangular markers is ≈ 30 nm. Blue dashed line shows an approximate height profile of the as-prepared well.

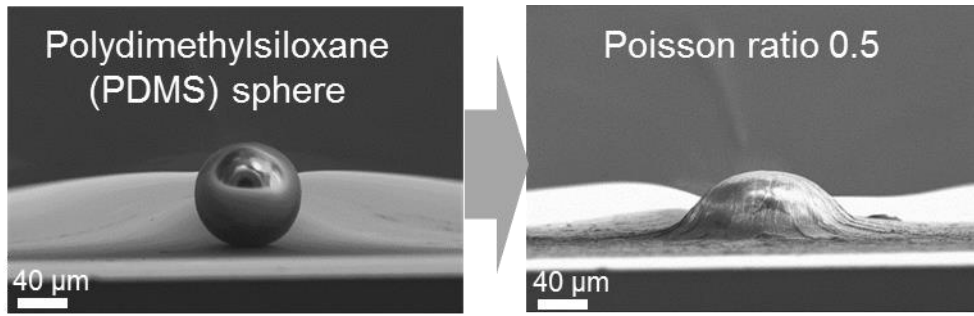


Figure S2. SEM image of the PDMS sphere before (left) and after (right) encapsulation with graphene oxide.

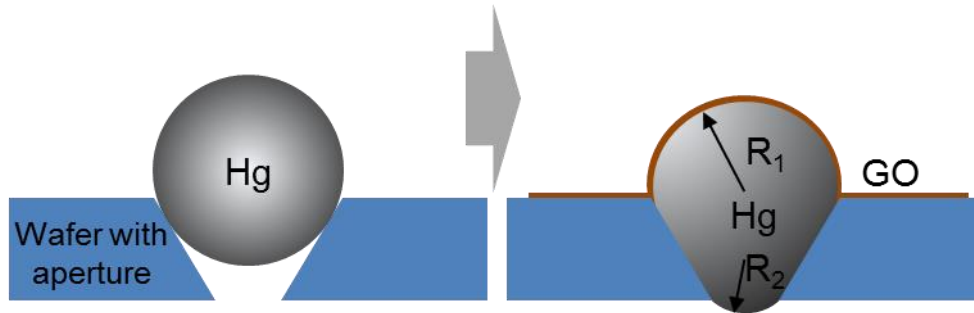


Figure S3. Scheme of the experiment to estimate the pressure induced by graphene oxide membrane on a liquid incompressible object. The pressure balance can be described as $\frac{2\gamma_{GO}}{R_1} + \frac{2\gamma_{Hg}}{R_1} = \frac{2\gamma_{Hg}}{R_2}$, where γ_{GO} , γ_{Hg} stand for the effective surface tensions of graphene oxide and Hg correspondingly; R_1 and R_2 are radii of drop curvatures from wide and narrow sides of the conical aperture, respectively. Measuring $R_1=268 \mu\text{m}$, $R_2=100 \mu\text{m}$ and taking $\gamma_{Hg}=0.487 \text{ N/m}$, we obtain $\gamma_{GO}=0.816 \text{ N/m}$ and pressure differential across the membrane ($\Delta p = \frac{\gamma_{GO}}{R_1}$) $\approx 4 \cdot 10^3 \text{ Pa}$. Therefore, the tensile stress applied to the 138 nm thick membrane is equal to 5.9 MPa.

TOC Figure

